Tilted-CAIPI for Highly Accelerated Distortion-Free EPI with Point Spread Function (PSF) Encoding

Zijing Dong[1], **Fuyixue Wang**[2,3], **Timothy G. Reese**[2], **Mary Kate Manhard**[2], **Berkin Bilgic**[2], **Lawrence L. Wald**[2,3], **Hua Guo**[1], and **Kawin Setsompop**[2,3,*]

[1]Center for Biomedical Imaging Research, Department of Biomedical Engineering, Tsinghua University, Beijing, China

[2]A. A. Martinos Center for Biomedical Imaging, Department of Radiology, Massachusetts General Hospital, Charlestown, MA, United States

[3]Harvard-MIT Health Sciences and Technology, MIT, Cambridge, MA, United States

Abstract

Purpose—To develop a method for fast distortion- and blurring- free imaging.

Theory—EPI with Point-Spread-Function (PSF) mapping can achieve distortion- and blurring-free imaging at a cost of long acquisition time. In this study, an acquisition/reconstruction technique, termed "*tilted-CAIPI*", is proposed to achieve >20× acceleration for PSF-EPI. The proposed method systematically optimized the k-space sampling trajectory with B_0-inhomogeneity-informed reconstruction, to exploit the inherent signal correlation in PSF-EPI and take full advantage of coil sensitivity. Susceptibility-induced phase accumulation is regarded as an additional encoding which is estimated by calibration data and integrated into reconstruction. Self-navigated phase correction was developed to correct shot-to-shot phase variation in diffusion imaging.

Methods—*Tilted-CAIPI* was implemented at 3T, with incorporation of partial Fourier and simultaneous multislice to achieve further accelerations. T_2-weigthed, T_2^*-weighted and diffusion-weighted imaging experiments were conducted to evaluate the proposed method.

Results—The ability of *tilted-CAIPI* to provide highly accelerated imaging without distortion and blurring was demonstrated through in-vivo brain experiments, where only 8 shots per simultaneous slice group were required to provide high-quality, high-SNR imaging at 0.8–1mm resolution.

Conclusion—*Tilted-CAIPI* achieved fast distortion- and blurring- free imaging with high SNR. Whole-brain T_2-weighted, T_2^*-weighted and diffusion imaging can be obtained in just 15–60s.

Keywords

---

*Correspondence to: Kawin Setsompop, Building 75, Room 2.102, 13th Street, Charlestown, MA, 02129, USA, kawin@nmr.mgh.harvard.edu.

INTRODUCTION

The fast acquisition speed of echo-planar imaging (EPI) has made it a commonly used MR sequence for many applications, such as in diffusion MRI (1) and functional MRI (2). However, due to its low encoding bandwidth along the phase encoding (PE) direction, single-shot EPI (SS-EPI) can suffer from severe susceptibility-induced geometric distortion and T_2^* blurring. These artifacts can lead to inaccurate structural assessment and loss in spatial resolution, limiting the image quality of EPI and its ability to obtain high resolution anatomical images.

To mitigate distortion and blurring, parallel imaging techniques (3,4) have been applied to SS-EPI to reduce the effective echo spacing (ESP). However, the levels of distortion and blurring that can be mitigated by parallel imaging are limited by the achievable acceleration (R_{PE}), where high accelerations could result in severe signal-to-noise ratio (SNR) loss and aliasing artifacts. As an alternative, a number of multi-shot EPI methods (5–8) have been developed to reduce the distortion of EPI while maintaining high SNR, but at a cost of prolonged scan time. Nevertheless, geometric distortion and blurring artifacts can still be significant even with a highly segmented multi-shot acquisition (e.g., 6–8 shots), particularly in high resolution imaging and in areas with large susceptibility variations. To achieve negligible distortion and blurring, a very large number of shots/segments are required for such approaches that can result in very long scan time (9).

For diffusion-weighted imaging (DWI), physiological motion during the application of diffusion gradients can cause strong background phase variations among different acquisition shots, which complicates the reconstruction of multi-shot EPI. In order to estimate and correct for such shot-to-shot phase variation, navigator-free methods (7,10) have been proposed based on parallel imaging. However, when a very large number of shots is utilized to achieve low distortion and blurring, the individual parallel imaging reconstruction of each shot at high R_{PE} that is used for self-navigation can be difficult to achieve. In such case, an extra 2D navigator acquisition might be necessary (11,12), leading to added acquisition time.

To achieve distortion- and blurring- free imaging with EPI, Point-Spread-Function (PSF) mapping (13,14) technique has been developed. PSF mapping encodes an additional phase-encoding (k_{psf}) into the EPI acquisition to provide a highly reliable mapping of the B_0-distortion and T_2^*-blurring. Due to its encoding-intensive nature, which typically requires >100 EPI shots for a single image (matrix size >100), PSF-encoded EPI (PSF-EPI) is mostly performed as a pre-scan, to estimate a distortion map used for post-processing correction of subsequent EPI scans(15,16). Such correction effectively removes the B_0-distortions, but does not remove the T_2^*-blurring and has difficulty recovering the loss of resolution and anatomical details in areas with strong susceptibility variations. Methods have been proposed to accelerate PSF-EPI by 5–8× through a combination of reduced-FOV$_{PSF}$ (rFOV) approach and parallel imaging along the PE direction (9), or along the PE and the PSF directions (17). This has recently permitted PSF-EPI to be used for imaging directly instead of as a pre-scan, to achieve very high-quality diffusion imaging at 3T and 7T without distortion and blurring artifacts (9). In (9), PSF-EPI was shown to have superior

performance when compared to readout-segmented EPI that still suffers from distortions at 31 segments acquisition. Nonetheless, even with such accelerations, 30–40 EPI-shots are still needed to acquire a single brain imaging slice at 1mm resolution. In addition, 2D navigator acquisition is required to correct for phase variations among different encoding shots in diffusion imaging, which further prolongs the scan time. Therefore, the long scan time of PSF-EPI still limits its practicability for diffusion MRI especially for high angular resolution diffusion imaging (HARDI) (18–20), and has limited its ability to outperform existing distortion-free anatomical scans such as T_2-weighted imaging by turbo spin echo (TSE) sequence.

In this study, we propose a novel acquisition/reconstruction technique, termed "*tilted-CAIPI*', to achieve >20× acceleration in PSF encoding for efficient distortion- and blurring-free imaging. The proposed method systematically optimizes the k-space under-sampling along the PSF and PE directions for B_0-inhomogeneity-informed parallel imaging reconstruction, which exploits the inherent signal correlation in the PSF-EPI data and take full advantage of coil sensitivity encoding. In the proposed B_0-inhomogeneity-informed reconstruction, susceptibility-induced phase accumulation along the PE direction of the EPI is regarded as an additional encoding information which is estimated by a calibration data and integrated into the parallel imaging reconstruction. The proposed *tilted-CAIPI* method was also combined with partial Fourier acquisition to achieve fast, distortion- and blurring-free imaging at the 0.8–1mm resolution range using only 8 acquisition shots per simultaneous slice group. For volumetric imaging, the proposed method was further combined with blipped-CAIPI simultaneous multislice (SMS) acquisition (21) to achieve efficient whole-brain T_2-weighted and T_2^*-weighted imaging. Lastly, for diffusion imaging, self-navigated acquisition and phase-corrected reconstruction were developed within the *tilted-CAIPI* PSF-EPI framework to correct the shot-to-shot phase variation. The ability of *tilted-CAIPI* to provide highly accelerated imaging without distortion and blurring was demonstrated through T_2-weigthed, T_2^*-weighted and diffusion-weighted brain imaging experiments at 3T.

THEORY

In this section, a brief review of PSF encoding in EPI is provided, followed by a detailed description of the proposed *tilted-CAIPI* acquisition and reconstruction scheme. Then, the section continues on with a description of the proposed self-navigated acquisition and phase-corrected reconstruction for self-navigated PSF-EPI in diffusion imaging.

EPI with PSF encoding (PSF-EPI)

PSF-EPI utilizes an additional phase-encoding dimension, PSF-encoding (k_{psf}), to acquire a distortion-free spatial dimension along *y*. As shown in Fig. 1a, a spin-warp gradient blip (PSF-encoding) along the phase-encoding (G_y) direction is applied before each EPI readout, and changes shot-to-shot to acquire the additional PSF-encoding dimension. The sequence loop of PSF-EPI with diffusion encodings is shown in Figure 1b. Through PSF-EPI, a 3D k-space (k_x-k_y-k_{psf}) is acquired for each imaging slice as shown in Fig. 2, where k_x is omitted. Here, the 2D k-space data (k_x-k_y) acquired at k_{psf}= 0 is the same as in the standard single-

shot EPI acquisition, and the k-space center of the other acquisition shots (i.e. at $k_{psf} \neq 0$) are shifted to the left/right relative to the $k_y = 0$ position by the PSF-encoding gradient blips. Since the ESP along the phase encoding direction of the EPI is much larger than that along the readout direction, the susceptibility-induced phase accumulation and T_2^* decay along k_y often lead to severe distortion and blurring along y, while the levels of distortion and blurring are negligible along the readout direction. In PSF-EPI, at a certain k_y position in k_y-k_{psf} space, all the PSF-encoding signals at different k_{psf} are acquired at the same echo time. Therefore, there is no distortion and blurring along the PSF direction.

In conventional accelerated PSF-EPI (17), PE-PSF (k_y-k_{psf}) encodings are undersampled by $R_{PE} \times R_{PSF}$ (Fig. 2a), and reconstructed by sequential PE-GRAPPA followed by either PSF-GRAPPA or reduced-FOV unfolding reconstruction. Since the y-psf dimension is close to a diagonal line in the image domain, rFOV unfolding can be directly used to recover the aliased image when R_{PSF} and distortions are not very large (9,17). Here, R_{PE} is used to reduce the effective ESP and thereby the level of distortion and blurring that needs to be encoded using PSF encoding. This in turn enables higher PSF accelerations and hence less EPI shots which reduces the acquisition time.

Tilted-CAIPI

To achieve higher accelerations for PSF-EPI, "*tilted-CAIPI*" is proposed to exploit the inherent signal correlation of PE and PSF encodings, through optimized sub-sampling and reconstruction. In PSF-EPI, PSF encoding utilizes a G_y pre-winding blip to shift the effective phase-encoding of each EPI-shot. Therefore, data points along a -45° diagonal line in the k_y-k_{psf} plane (Fig. 2) share the same effective G_y-gradient encoding. The differences between the signals on the same k_y-k_{psf} diagonal line are (i) B_0-inhomogeneity induced phase and (ii) T_2^* decay (and/or T_2' recovery). Since the differences of encoding time are very small among neighboring points along such a diagonal line (a few milliseconds), a tilted compact kernel in k_y-k_{psf} across multi-coil data should be able to effectively capture the small B_0-inhomogeneity induced phase and interpolate small T_2^* decay/T_2' recovery. Thus, undersampled data in a tilted kernel (Fig. 2b) along k_y-k_{psf} can be recovered by a weighted combination of its neighboring points across a multi-channel dataset that have close or the same G_y-gradient encodings, and small differences in B_0-inhomogeneity induced phase and T_2^* decay/T_2' recovery. To utilize the PSF-PE signal correlation in PSF-EPI, the kernel is tilted to the −45° diagonal direction along k_y-k_{psf}, and to make full use of coil sensitivity encoding, a tilted version of 2D-CAIPIRINHA (22) under-sampling pattern is proposed (Fig. 2c), which we termed *tilted-CAIPI*. The accompanying GRAPPA-like (4) interpolation process for *tilted-CAIPI* reconstruction can be expressed as,

$$d_i\left(k_x, k_y, k_{psf}\right) = \sum_{i'=1}^{N_c} \sum_{(k'_x, k'_y, k'_{psf}) \in \mathbf{K}} w_i\left(i', k'_x - k_x, k'_y - k_y, k'_{psf} - k_{psf}\right) d_{i'}\left(k'_x, k'_y, k'_{psf}\right), \quad [1]$$

where $d_i(k_x, k_y, k_{psf})$ is the to-be-interpolated k-space data at k_x-k_y-k_{psf} location of the i-th channel, $\mathbf{d}_{i'}(k'_x, k'_y, k'_{psf})$ is the acquired data point in the tilted kernel (denoted by $\mathbf{K}$), w are interpolation weights of this specific kernel pattern, and N_c is the number of channels. The weights used here in *tilted-CAIPI* contain both the coil sensitivity and correlation of k_y-k_{psf} encoding, with additional encoding information from B_0-inhomogeneity induced phase. A calibration data is required to train the kernel weights for such PSF-PE GRAPPA reconstruction. Such calibration data need to be fully-sampled or recovered via PE-GRAPPA to full sampling along k_y-k_{psf}, and should be acquired over a sufficiently large k-space region to provide enough data for accurate kernel fitting.

The correlation of PE and PSF encoding and the rationale of the B_0-inhomogeneity-informed reconstruction can be explained through the following analysis in image domain. If a gradient-echo EPI is used, the 2D image (*x-psf*) at $k_y = k_m$, I_m can be expressed as:

$$I_m = I_0 e^{-m\Delta t/T_2^*} e^{-i\vec{k}_m \vec{y}} e^{i\gamma\Delta B m\Delta t}. \quad [2]$$

Here, m is the index of k_y which starts at 0 for $k_y = -k_{ymax}$, I_0 is the image at the first echo (m=0, k_y=$-k_{ymax}$), Δt is the echo spacing along k_y, $e^{-m\Delta t/T_2^*}$ is the T_2^* signal decay term, $e^{-i\vec{k}_m\vec{y}}$ is the phase encoding modulation, and $e^{-i\gamma\Delta B m\Delta t}$ is the susceptibility-induced phase accumulation, where ΔB is the B_0-inhomogeneity. I_m is free from distortion and blurring because the susceptibility-induced phase accumulation and T_2^* decay are the same across all of the signals along the PSF-encoding direction. Based on Eq. [2], the correlation between two distortion-free images, I_m and I_n, at two different echo times can be represented by,

$$I_n = I_m e^{-(n-m)\Delta t/T_2^*} e^{-i(\vec{k}_n - \vec{k}_m)\vec{y}} e^{-i\gamma\Delta B(n-m)\Delta t}. \quad [3]$$

In this equation, $e^{-i(\vec{k}_n - \vec{k}_m)\vec{y}}$ is a linear phase caused by the shift of G_y-gradient encoding in PSF-EPI, $e^{-(n-m)\Delta t/T_2^*}$ and $e^{-i\gamma\Delta B(n-m)\Delta t}$ are the difference of T_2^* decay and B_0-inhomogeneity induced phase due to the different echo times of I_m and I_n. If m-n is small, $e^{-(n-m)\Delta t/T_2^*}$ is approximate to 1, and the linear phase along y is known and can be eliminated by shifting the k-space along k_{psf} (i.e. tilted kernel). Therefore, the correlation between I_n and I'_m that has been shifted in k-space can be simplified to:

$$I_n \approx I'_m e^{-i\gamma\Delta B(n-m)\Delta t} \quad [4]$$

The only difference here is the B_0-inhomogeneity induced phase. This phase accumulation is relatively smooth in the image domain and can be regarded as an additional encoding that

can be estimated by a convolutional operator in k-space. In the proposed k-space reconstruction, the small T_2^* decay is approximated via a linear interpolation of data in the neighborhood of points in the compact GRAPPA kernel, while the shift along k_{psf} corresponds to the tilt of the kernel along k_y-k_{psf}.

In Eq. [4], the difference of B_0-inhomogeneity induced phase is determined by ΔB, Δt, and (n-m), and smaller values of the three parameters result in higher correlation of k-space signals. Thus, a reduced effective ESP (Δt) allows larger interpolation distance (n-m) (larger R_{PSF}) for a given level of ΔB. In *tilted-CAIPI*, the effective ESP is reduced by under-sampling along PE (R_{PE}), and the joint reconstruction of PSF-PE with 2D CAIPI pattern (Fig. 2c) can help achieve a larger R_{PE} than conventional sampling by using the data at different k_{psf} with complementary G_y-gradient encoding in the reconstruction.

To train the kernels for PSF-PE GRAPPA, the calibration data should be acquired with the same effective ESP and ΔB as the actual imaging scan. If the effective ESP of the imaging scan is very small from using a large R_{PE} (e.g., 4), the effective ESP of the calibration scan cannot be easily reduced to the same value while retaining single shot acquisition by reducing the imaging resolution along the readout direction due to ramp-sampling limitation of the EPI readout. In this case, both a reduction in the readout resolution and PE under-sampling (e.g., at R_{PE}=2) are used to obtain a calibration dataset at the same effective ESP as the imaging acquisition. The undersampled calibration data at small R_{PE} can be recovered to full sampling through standard PE-GRAPPA reconstruction before used for PSF-PE GRAPPA training.

It can be time consuming to acquire all of the fully-sampled PSF-encoding shots required to train the PSF-PE GRAPPA kernels at large R_{PSF}, even if the calibration data is acquired across a limited range of k_{psf}. To reduce the number of acquisition shots (k_{psf}) in the calibration data, the number of different kernels that needs to be trained can be reduced if the undersampled PSF-EPI data is only to be partially recovered by PSF-PE GRAPPA as shown in Fig. 2d, and then unfolded by rFOV unfolding method (9,17) in the image domain. Through this approach, the number of different kernels in PSF-PE GRAPPA is reduced along k_{psf} and the calibration data can be undersampled along the PSF direction by R_{rFOV}.

For the actual PSF-EPI acquisition, to further reduce the acquisition time, *tilted-CAIPI* can be combined with blipped-CAIPI SMS (21) and partial Fourier acquisition. The reconstruction framework for such an acquisition is illustrated in Fig. 3B. The steps in the dashed boxes are only required for diffusion imaging, to correct for shot-to-shot phase variation. In this reconstruction framework, slice-GRAPPA is first applied to separate the data of the simultaneously acquired slices for both the imaging and the calibration data. The slice-unaliased PE-undersampled calibration data is then reconstructed using PE-GRAPPA, and used for the kernel training of PSF-PE GRAPPA. Note that slice- and PE- GRAPPA kernels are trained using conventional training data that is also acquired as a pre-scan using FLEET acquisition with 48 PE lines (23). After PSF-PE GRAPPA reconstruction, a less undersampled 3D k-space is obtained (k_x-k_y are now fully sampled and k_{psf} is less undersampled), and 3D POCS algorithm is applied to reconstruct the missing partial Fourier data along PSF and PE. Finally, rFOV unfolding is utilized in the image domain to generate

the aliasing-free 3D image (*x-y-psf*). Distortion-free images can then be obtained by combining image data along the PE direction using sum-of-square (SOS) (9), while distorted image is obtained through the SOS along the PSF direction.

Self-navigated phase correction for DWI

A big challenge in multi-shot DWI is the shot-to-shot image phase corruption due to physiological motion during the diffusion encoding. To correct for such shot-to-shot phase corruption among the different PSF encoding shots in PSF-EPI, a self-navigated phase correction method is proposed. As shown in Fig. 3A, each PSF-encoding shot contains a portion of the 2D low-frequency k_x-k_y signals (marked by wiggly signals, k_x is omitted), which can be used to estimate the image phase of that shot. The estimated phase of non-diffusion-weighted image at $k_{psf} = k_m$ (*m*-th shot) is,

$$P_{k_m}^{b\,=\,0} = P_{background} + \gamma\Delta B \times TE_m, \quad [5]$$

where $P_{background}$ is the background phase, and TE_m is the echo time of k-space center at $k_{psf} = k_m$. The image phase of the diffusion-weighted image at the same PSF-encoding position ($k_{psf} = k_m$) is,

$$P_{k_m}^{DWI} = P_{background} + \gamma\Delta B \times TE_m + P_{diffusion} + \gamma\Delta B_{eddy-current}TE_m. \quad [6]$$

Here, $P_{diffusion}$ is the diffusion phase, and $\Delta B_{eddy-current}$ is the field off-resonance caused by eddy-current. The subtraction of these two estimated phase is

$$P_{k_m}^{DWI} - P_{k_m}^{b\,=\,0} = P_{diffusion} + \gamma\Delta B_{eddy-current}TE_m. \quad [7]$$

Since our target diffusion imaging with PSF-EPI will be at high spatial resolution, where we aim to use a relatively low b-value (b=1000s/mm^2) to preserve SNR, we have observed that the eddy-current induced phase $\gamma\Delta B_{eddy-current}\,TE_m$ for such acquisition is much smaller when compared to the diffusion phase $P_{diffusion}$ and therefore will be ignored here (see Figure S1 in Supporting Information). With this assumption, the diffusion-induced phase variation of each PSF-encoding can be estimated directly using Eq. [7]. Note that as the PSF-encoding shifts the k-space center of each PSF-EPI acquisition shot, the last several shots at large negative k_{psf} encodings could lose the low-frequency information needed to estimate $P_{diffusion}$ (Fig. 3A). To compensate for the missing low-frequency signals, extra-sampling of PE lines (3 lines in this study) at the end of readout is implemented as shown in Fig. 1 & 3A.

Since a joint PSF-PE GRAPPA reconstruction across k_y-k_{psf} is used in *tilted-CAIPI*, shot-to-shot phase variation needs to be accounted for prior to the reconstruction. As shown in Fig. 3B, the phase corruption of each PSF encoding is estimated by first reconstructing each shot individually through conventional slice- and PE- GRAPPA and passing the reconstructed image phase through Eq. [7]. The estimated phase of each PSF-encoding is then added into the calibration data as additional information to train for in the PSF-PE GRAPPA kernels for each DWI volume. Since the phase corruption changes from shot to shot, the kernel spanning different PSF encodings should be trained by a new phase-corrected calibration data with added diffusion phases that are estimated from the corresponding shots.

After PSF-PE GRAPPA reconstruction, the PSF-EPI data are now fully-sampled along the PE direction, and the diffusion phase corruption in each shot can be removed directly in image domain, using previously estimated phase corruption. However, since the estimated phase corruptions contain eddy-current induced phase contributions, this correction step also adds the eddy-current phase back into the PSF encodings. Thus, the resultant PSF dimension will have the same eddy-current-induced distortion as in the PE direction. For the target acquisition at relatively low b-values and high R_{PE}, such eddy-current distortion is relatively small but still can lead to mismatches between different diffusion directions. Such eddy-current distortion can be corrected for through standard post-processing methods such as *eddycorrect* in FSL (24,25), where the loss in resolution from the spatial interpolation used in such correction is expected to be very small given the small eddy-current distortions in our target acquisitions. For higher b-value acquisitions with larger eddy-current distortions, to avoid blurring due to spatial interpolation, the eddy-current induced off-resonance can be estimated by a phantom pre-scan or by the reconstructed images itself using FSL. The corresponding eddy-current phase can then be calculated and removed from Eq. [7] for accurate estimation of diffusion phase in the proposed phase correction step. This will allow for a direct reconstruction of PSF-EPI that is free of eddy-current distortion as shown in Fig. S2a.

METHODS

All in-vivo experiments were conducted on a Siemens 3T Prisma scanner on healthy volunteers, following approval by an Institutional Review Board and obtaining written informed consent. To evaluate the performance of *tilted-CAIPI* at various acceleration factors, a PSF SE-EPI data containing both non-diffusion-weighted and diffusion-weighted images were acquired with $R_{PSF}=2$ (Table 1, scan 1). The data were then retrospectively undersampled along the PSF direction to generate datasets with larger R_{PSF} factors for testing and evaluation. In all cases, data were created to have a *tilted-CAIPI* sampling pattern, with complementary k_y under-sampling between different PSF encoding shots. Under-sampling along PE ($R_{PE}=4$) was used to reduce the effective ESP to 0.245ms for this acquisition with 1 mm in-plane resolution, and the calibration data were acquired at a lower resolution of 3.4mm with $R_{PE}=2$ to achieve the same effective ESP as the 1mm imaging scan. Data with different partial Fourier factors were also generated to evaluate the POCS reconstruction and the image error caused by partial Fourier acquisition.

High-resolution whole-brain T_2-weighted (Table 1, scan 2) and T_2^*-weighted (Table 1, scan 3) imaging were performed using spin-echo EPI and gradient-echo EPI, respectively, in order to validate the ability of the proposed method to remove both distortion and blurring artifacts. A high acceleration factor of $R_{PSF} \times R_{PE}=22 \times 4$ with *tilted-CAIPI* was applied together with partial Fourier = 0.67 along the PSF-encoding direction, that reduced the number of acquisition shots from 244 to just 8 per simultaneous slice group, corresponding to a 30.5× acceleration in PSF encoding. SMS was also used to further accelerate these whole-brain scans through a multiband (MB) acceleration of 2. With this acquisition strategy, the total scan time for the $0.9 \times 0.9 \times 1$ mm^3 T_2-weighted imaging with whole-brain coverage was 52s, with an added calibration scan time of 1min. For T_2^*-weighted imaging, the slice thickness of 3mm was used along with a 0.8×0.8 mm^2 in-plane resolution, thus the acquisition time was even shorter, at 15s for the imaging scan and 16s for the calibration scan. A whole-brain MPRAGE dataset at $1 \times 1 \times 1$ mm^3 resolution was also acquired to provide a distortion-free reference to compare with the T_2-weighted imaging from PSF-EPI.

The effectiveness of self-navigated phase correction was first validated using the DWI data (Table 1, scan 1). Three extra PE lines were acquired at the end of the EPI readout of each PSF encoding to achieve self-navigation, as per Fig. 3A. Since $R_{PE}=4$ was employed, the 3 additional PE lines were reconstructed to provide 12 k-space lines, and the size of the self-navigator data was set to be a symmetric 24-lines along PE. Non-diffusion-weighted calibration data with added estimated phase of each PSF encoding (as described in the theory section) were used to train the PSF-PE kernels for all diffusion directions. In-vivo diffusion experiment (Table 1, scan 4) was also performed for HARDI acquisition with 48 diffusion directions at b=1000 s/mm^2 (4 of them are b = 0 images). The image resolution for this acquisition was $0.8 \times 0.8 \times 3$ mm^3 with whole-brain coverage. A total acceleration of 61× ($R_{PSF} \times PF_{PSF} \times MB$) was achieved through the combination of *tilted-CAIPI* ($R_{PSF}/R_{PE}=22/4$), partial Fourier acquisition ($PF_{PSF}=0.67$) and SMS (MB=2). Through this high acceleration, the total acquisition time for the HARDI scan was 19 minutes and 40s (19min12s imaging scan + 28s calibration acquisition).

To evaluate the described approach for integrated eddy-current distortion correction in the PSF reconstruction rather than in post-processing, DW phantom data were acquired under $R_{PSF} \times R_{PE}=22 \times 2$ (Table, scan 5), where the smaller R_{PE} was used to create a larger amount of eddy-current distortion that needs to be corrected. The eddy-current induced phase was calculated using the parameters estimated from FSL with a linear eddy-current model, and the framework and results for integrated eddy-current correction are shown in Fig. S2a.

For data acquisition, the DWI data (Table 1, scan 1) were acquired using a custom-built 64-channel radiofrequency head array (26), while the other datasets (Table 1, scan 2–5) were all acquired using a Siemens 32-channel head coil array.

The reconstruction framework from Fig. 3B was used for all reconstructions. The kernel size for PSF-PE GRAPPA was set to $7 \times 4 \times 2$ ($k_x \times k_y \times k_{psf}$). For DWI acquisitions, the diffusion phases estimated by the self-navigation were filtered by a hamming window to improve SNR. For the diffusion imaging reconstruction with PSF-PE GRAPPA, a set of PSF-PE kernels were trained specifically for each pair of PSF-encodings where the kernel size was 2

along k_{psf}. This was done to ensure that the correct shot-to-shot diffusion phase differences were embedded into the kernels in each reconstruction case. For example, 7 sets of kernels were trained for each 8-shot acquisition of a given diffusion direction, each kernel trained using calibration data with different added phases obtained from the two corresponding shots. The number of iterations for POCS partial Fourier reconstruction was set to 6 which was observed to be sufficient to achieve convergence. FSL (24,25) was used for registration, eddy-current correction and tensor fitting for diffusion imaging.

RESULTS

Figure 4 shows the reconstructed non-DW images from the first dataset (Table 1, scan 1). In Fig. 4A, three different reconstruction methods: rFOV unfolding, PSF-GRAPPA with a square kernel, and the proposed *tilted-CAIPI* with PSF-PE GRAPPA were compared at R_{PSF}=6 and 22. All of the three methods were able to reconstruct the PSF-undersampled data to generate distortion-free images at R_{PSF}=6, while only the *tilted-CAIPI* method performed well without artifacts at R_{PSF}=22. The cause of the artifacts in the rFOV unfolding reconstruction is illustrated in Fig. 4C, where the diagonal image line can only be recovered if the reduced FOV (between the two diagonal dashed lines) is still large enough to keep all the distorted pixels from wrapping. At R_{PSF}=22, the FOV was too small and the distortion along y resulted in fold-over signals that cannot be recovered by rFOV unfolding. For PSF-GRAPPA with a square kernel, the reconstruction at R_{PSF}=22 is too ill-conditioned, resulting in large artifacts. Compared to the distortion-free images from PSF-EPI with *tilted-CAIPI*, the image produced by SS-EPI at R_{PE} = 4 shows severe distortions at the air-tissue boundaries (Fig. 4B), even when the effective ESP has already been reduced by parallel imaging to 0.245ms. Figure 5 shows the results of POCS partial Fourier reconstruction using this dataset (Table 1, scan 1) at PF_{PSF}=12/12, 10/12 and 8/12. The undersampled data at R_{PSF}=22 was reconstructed by PSF-PE GRAPPA first, and then recovered by POCS partial Fourier reconstruction. Through POCS reconstruction, the reconstruction errors from using partial Fourier acquisition are relatively small (nRMSE < 4%).

Results of T_2-weighted images from *tilted-CAIPI* PSF-EPI (Table 1, scan 2) are shown in Fig. 6. Two representative slices are shown, along with the corresponding distortion-free MPRAGE images at the same slice positions. Results from SS-EPI acquired with R_{PE} = 4 are also shown, where severe distortions (yellow arrows) are observed when compared with the MPRAGE images. In contrast, the brain boundaries in images from PSF-EPI and MPRAGE are identical even near the eye ball where a large susceptibility variation is present. This demonstrates the ability of PSF-EPI with *tilted-CAIPI* to achieve high-quality distortion-free imaging even at a very high acceleration factor of R_{PSF}=22. Moreover, the images acquired by *tilted-CAIPI* PSF-EPI achieved a much higher SNR than those of SS-EPI, without visible aliasing artifacts and high noise amplification caused by g-factor penalty in the SS-EPI case.

Figure 7 shows the reconstructed $T_2{}^*$-weighted PSF-EPI image data (Table 1, scan 3) that has been combined along the y dimension to create *psf-x* images (top-row), and along the *psf* dimension to create *y-x* images (bottom-row). With *tilted-CAIPI*, data in both *psf-x* and *y-x* planes achieved high SNR and high resolution. However, as expected, the distorted

images in the *y-x* plane are more blurred along the A-P (*y*) direction when compared to the distortion-free and blurring-free image in the *psf-x* plane, even $R_{PE}=4$ was used for blurring reduction. The differences of effective resolution in these images can be appreciated in the zoomed-in regions.

Figure 8 shows the comparison between SS-EPI, PSF-EPI without phase correction, PSF-EPI with self-navigated phase correction, and highly-accelerated PSF-EPI with *tilted-CAIPI* using the data from the DWI scan (Table 1, scan 1). As can be seen in Fig. 8, the 108-shot PSF-EPI acquisition was able to nicely eliminate the susceptibly-induced distortion that exists in SS-EPI, and the strong aliasing artifacts caused by shot-to-shot phase corruption were effectively eliminated by the proposed self-navigation approach. The highly-accelerated *tilted-CAIPI* PSF-EPI acquisition was also able to generate distortion-free DW images with high quality that is close to the 108-shot PSF-EPI, but acquired using just 8-shots in a much shorter acquisition time. The results of axial DTI scan (Table 1, scan 4) were presented in Fig. 9. Distortion- and blurring- free images from non-DW and DW acquisitions were shown along with color-coded fractional anisotropy (FA) maps. Through *tilted-CAIPI* acceleration, PSF-EPI was used to obtain these high-SNR high-resolution diffusion images with detailed structures at a temporal resolution of 24s/per direction. The results of the phantom acquisition (Table 1, scan 6) can be found in the Supporting Information (Fig. S2b), where the eddy-current induced distortion was effectively mitigated by *tilted-CAIPI* with the integrated eddy-current corrected phase estimation approach (Fig. S2a).

DISCUSSION

In this study, the *tilted-CAIPI* acquisition/reconstruction was proposed and used to obtain high-quality highly-accelerated PSF-EPI data. To achieve this, the proposed method carefully exploited the inherent signal correlation in the PSF-EPI data across the PSF and PE dimensions using a new CAIPI under-sampling scheme and a new GRAPPA-like reconstruction with tilted kernels to take advantage of the B_0-inhomogeneity information. The ability of the proposed *tilted-CAIPI* to achieve distortion- and blurring- free imaging under high accelerations ($R_{PSF}=22$, $R_{total}=61$) was demonstrated through T_2-weighted (Fig. 6), T_2^*-weighted (Fig. 7) and diffusion-weighted imaging (Fig. 8&9) experiments. With such acceleration, only 8 acquisition shots per simultaneous slice group were required for high-quality brain imaging at the 0.8–1mm resolution range, which should prove useful for a number of applications where rapid anatomical imaging and high-quality diffusion imaging are desired.

In *tilted-CAIPI*, the achievable R_{PSF} depends on the level of B_0 inhomogeneity and effective echo spacing. The use of a high R_{PE} acceleration reduces the effective ESP and allows for a higher R_{PSF} acceleration to be used in the PSF-encoding to reduce the scan time. However, the achievable R_{PE} is limited by the ill-conditioning of parallel imaging at high accelerations. Through the use of *tilted-CAIPI* PSF-PE under-sampling and joint PSF-PE GRAPPA reconstruction, a high R_{PE} of 4 was achieved with high-quality reconstruction for acquisitions at 3T using either a 32- or 64- channel head coil, to allow for a high $R_{PSF}=22$ to be used. Note that the conventional sequential reconstruction with PE-GRAPPA and PSF-

GRAPPA will not be able to take advantage of the complementary sampling provided by *tilted-CAIPI*, since the reconstructed k-space points from PE-GRAPPA would have already contained substantial noise and bias that will affect the subsequent PSF-GRAPPA reconstruction. The SNR of PSF-EPI with *tilted-CAIPI* is reduced by $\sqrt{R_{PSF}}$ compared to full sampling, and g-factor noise amplification could increase at high acceleration factors. G-factor quantification of *tilted-CAIPI* is not straight-forward since it depends on both coil sensitivity and the spatially varying B_0-inhomogeneity, and this quantification will be an important future direction of our work. Given that the achievable acceleration factor (R_{PSF}) is high, the $\sqrt{R_{PSF}}$ penalty will be large. However, a significant SNR boost that counteracts this lost is expected from the much longer acquisition window of PSF-EPI (50–70ms used in this work) when compared to e.g. traditional spin-warp counterparts of 5–10ms. To allow for even higher R_{PSF}, a stronger gradient hardware system with higher gradient amplitude and slew rate would be helpful as it would further reduce ESP, but peripheral nerve stimulation must also be taken into consideration for safety.

The *tilted-CAIPI* kernel spans a larger k-space width than conventional GRAPPA. However, a time width of 5–6 ms is still maintained across the kernel, and only minor T_2^* signal decay should arise during this time for typical brain tissue species which should not cause reconstruction artifacts. However, for signals with very short T_2^* and/or in the case of larger effective ESP and time width, potentially residual aliasing artifacts similar to ones caused by T_2 decay in the virtual coil GRAPPA work for TSE acquisition (27) could occur. In such case, a similar Tikhonov regularization approach as employed by Blaimer et al. could be explored to suppress the artifacts.

A calibration scan is required for *tilted-CAIPI* to obtain a training dataset with the same susceptibility and coil sensitivity information as in the actual imaging scan. To reduce the acquisition time needed for calibration scan, we proposed a strategy as shown in Fig. 2d in which PSF-PE GRAPPA is used to partially recover the missing k-space data, and the rFOV approach is used in the subsequent unfolding to reconstruct a clean image. Using this approach, the calibration data can be acquired with under-sampling along the PSF-encoding direction. The reduction factor used in the calibration data is determined by the limit of the rFOV unfolding approach, which depends on the effective ESP and the level of B_0-inhomogeneity (9). In our study, a conservative R_{rFOV} of 2 was used, however, a larger R_{rFOV} of up to 5 should be feasible for brain imaging at 3T to further reduce the acquisition time. In addition, a single calibration can be used to reconstruct multiple imaging scans with different contrast preparations and/or resolutions, as long as they have the same effective ESP, B_0-inhomogeneity, imaging FOV and positioning. For example, another spin-echo T_2-weighted scan was also acquired (which is not shown here) using the same parameters as the T_2^*-weighted scan (Table 1, scan 3), including FOV, resolution, ESP, and shimming. The data from this scan were successfully reconstructed using the gradient-echo calibration data. Moreover, the 48-direction diffusion dataset was also reconstructed using a single calibration scan without diffusion encoding. Thus, a calibration scan of less than 1 minute can be utilized for multiple contrast imaging in *tilted-CAIPI*.

In *tilted-CAIPI* PSF-EPI, partial Fourier along the PSF direction was used to further accelerate the acquisition, and partial Fourier along the PE direction was used to improve SNR through TE reduction. POCS algorithm was employed for partial Fourier reconstruction to iteratively reconstruct the missing data along both PE and PSF. Note that when partial Fourier is applied along both PE and PSF, the left-bottom and right-top regions of the k_y-k_{psf} data (in Fig. 3A) cannot be recovered well since its corresponding conjugate symmetric signals are missing. However, this did not seem to affect the reconstructed image significantly at our chosen partial Fourier acceleration factors as demonstrated in Fig. 5, but would likely to become more of an issue at higher partial Fourier factors. Alternatively, reduced resolution method can be used to reduce TE, in conjunction with the use of an extra navigator instead of self-navigation for phase estimation as per (9). This would avoid performing PF in both PE and PSF directions. Nonetheless, the reduced resolution approach would also result in a shorter acquisition window for imaging when compare to the partial Fourier approach, with less data points obtained for imaging after TE. This would reduce noise averaging and lower the SNR of the imaging scan. In this work, SMS was also employed at MB=2 to provide further acceleration to the target whole-brain acquisitions, where the overlapping data of the simultaneously acquired slices were untangled using slice-GRAPPA prior to the PE-PSF GRAPPA reconstruction. As part of our future work, to achieve higher MB accelerations, we plan to explore the use of tilted 3D-CAIPI under-sampling patterns across the PSF-PE-slice dimensions and develop a corresponding joint PSF-PE-slice GRAPPA reconstruction.

For diffusion imaging acquired using *tilted-CAIPI* PSF-EPI, the proposed self-navigation method improves the acquisition efficiency and was shown to effectively correct for shot-to-shot phase variation (Fig. 8). Such phase variation depends on the degree of physiological motion and b-values. The proposed phase-corrected reconstruction worked well in this study where the corrupted image phases are relatively smooth spatially since low b-value is used to allow high spatial resolution imaging with reasonable SNR. For higher b-values acquisitions, larger phase changes could occur to cause more variability in the conditioning and reconstruction performance, and the use of a lower R_{PSF} acceleration might be needed. Moreover, if large motion happens during the diffusion encoding gradients, data corruption could also occur and result in image deterioration. In such case, data rejection and motion compensation might be needed to maintain the image quality (28,29). The distortion-free images with high SNR that were acquired using PSF-EPI was shown to provide accurate structural details, and the large acquisition efficiency/acceleration gain through *tilted-CAIPI* enables high-resolution whole-brain HARDI acquisition to be perform in a reasonable time-frame. In diffusion imaging, different eddy-current induced distortions of different diffusion encodings need to be corrected for, before the subsequent diffusion processing. For diffusion acquisition, which was performed at a relatively low b-value of 1000 s/mm^2 and at a short effective ESP of ~0.25ms, the distortion from eddy-current was relatively mild. As such, a post-processing correction via the *eddycorrect* function in FSL was used (24,25), since the loss in resolution/blurring from the associated spatial interpolation should be negligible. Nonetheless, for higher b-value acquisitions with larger eddy current distortions, a more involved correction method described in Supporting Information (Fig. S2a) that incorporates the eddy-current information directly into the PSF reconstruction could be used to avoid the

loss in resolution from post-processing. However, such method still relies on the eddy-current field estimates from a post-processing correction algorithm, which might not account for higher order terms or temporal field variations across the readout. To thoroughly account for eddy-current, a navigator acquisition can be acquired at a cost of a longer scan time, to provide an unbiased diffusion phase estimate which will allow PSF-EPI to be reconstructed without eddy-current distortions. However, this is probably not necessary in most circumstances.

In relating to eddy currents, we also note that the calibration data for PSF-PE GRAPPA are obtained without diffusion encoding and hence contain different eddy-current induced off-resonance. As such, the temporal phase evolution across the EPI readout of the calibration data will be slightly different from that of the diffusion-weighted data. Nonetheless, the trained kernels have been demonstrated to work well in our diffusion acquisition, since the extra phase evolution from eddy-current is much smaller than the phase evolution from B_0 inhomogeneity that the kernel is encoding and is under the tolerance of such GRAPPA kernel-based interpolation/reconstruction.

There are a couple of restrictions in applying PSF-EPI with *tilted-CAIPI* to accelerate classic spin-warp PE sequences, in terms of minimum achievable TE and readout duration. These restrictions depend on R_{PE}, R_{PSF}, and echo spacing. For example, for $R_{PE}=4$, $R_{PSF}=22$ and echo spacing ~1ms used in this work, there should be at least 6 k_y points both before and after TE to allow the *tilted-CAIPI* kernel to work. The synergistic combination of wave-CAIPI (30) and *tilted-CAIPI* could potentially enable higher accelerations, as well as alleviated minimum TE and readout duration restrictions. However, the high EPI readout bandwidth will pose a limitation on the amount of wave encoding (31) and an extension to GRAPPA-based wave-CAIPI reconstruction (32) will also need to be made to incorporate *tilted-CAIPI*.

Tilted-CAIPI provides a new approach for distortion-free anatomical imaging that once implemented across different magnetization preparation sequences should enable for a rapid high-quality multi-contrast MRI exam. In this work, the proposed B_0-inhomogeneity-informed reconstruction was implemented in k-space by a GRAPPA-like reconstruction. More advanced reconstruction approaches that can take advantage of low-rank property (33) and/or joint-mutual information across a multi-contrast data (34) will also be explored in our future work to further improve reconstruction performance and enable even higher accelerations. With the *tilted-CAIPI* application in diffusion imaging, we have demonstrated distortion-free HARDI acquisition in a reasonable time-frame, and our future work will seek to incorporate *tilted-CAIPI* into our SNR-efficient gSlider acquisition (35) to achieve high-quality, distortion-free sub-millimeter isotropic diffusion MRI.

CONCLUSION

The proposed *Tilted-CAIPI* method achieves high acceleration for PSF-EPI through exploiting the inherent signal correlation across the PSF-PE encodings, using an optimized under-sampling scheme and a B_0-inhomogeneity-informed multi-coil reconstruction. The ability of *tilted-CAIPI* to achieve fast distortion- and blurring- free imaging with high SNR

was demonstrated in which brain data at the 0.8–1mm resolution range can be obtained using just 8 acquisition shots per simultaneous slice group, with 15–60s acquisition time for whole-brain T_2/T_2^*-weighted imaging. *Tilted-CAIPI* PSF-EPI with self-navigation was also proposed for diffusion imaging and was demonstrated to be effective in removing diffusion phase corruption. With this approach, high-resolution high-SNR DWI across 48 diffusion directions can be acquired in ~20 minutes, allowing for accurate diffusion imaging which should prove useful in neurosurgery and neuroimaging.

Supplementary Material

Refer to Web version on PubMed Central for supplementary material.

Acknowledgments

References

1. Warach S, Gaa J, Siewert B, Wielopolski P, Edelman RR. Acute human stroke studied by whole brain echo planar diffusion-weighted magnetic resonance imaging. Ann Neurol. 1995; 37:231–241. [PubMed: 7847864]

2. Biswal B, Zerrin Yetkin F, Haughton VM, Hyde JS. Functional connectivity in the motor cortex of resting human brain using echo-planar mri. Magn Reson Med. 1995; 34:537–541. [PubMed: 8524021]

3. Pruessmann KP, Weiger M, Scheidegger MB, Boesiger P. SENSE: sensitivity encoding for fast MRI. Magn Reson Med. 1999; 42:952–962. [PubMed: 10542355]

4. Griswold MA, Jakob PM, Heidemann RM, Nittka M, Jellus V, Wang J, Kiefer B, Haase A. Generalized autocalibrating partially parallel acquisitions (GRAPPA). Magn Reson Med. 2002; 47:1202–1210. [PubMed: 12111967]

5. Wang FN, Huang TY, Lin FH, Chuang TC, Chen NK, Chung HW, Chen CY, Kwong KK. PROPELLER EPI: an MRI technique suitable for diffusion tensor imaging at high field strength with reduced geometric distortions. Magn Reson Med. 2005; 54:1232–1240. [PubMed: 16206142]

6. Holdsworth SJ, Skare S, Newbould RD, Bammer R. Robust GRAPPA-accelerated diffusion-weighted readout-segmented (RS)-EPI. Magn Reson Med. 2009; 62:1629–1640. [PubMed: 19859974]

7. Chen NK, Guidon A, Chang HC, Song AW. A robust multi-shot scan strategy for high-resolution diffusion weighted MRI enabled by multiplexed sensitivity-encoding (MUSE). NeuroImage. 2013; 72:41–47. [PubMed: 23370063]

8. Dong Z, Wang F, Ma X, Zhang Z, Dai E, Yuan C, Guo H. Interleaved EPI diffusion imaging using SPIRiT-based reconstruction with virtual coil compression. Magn Reson Med. 2018; 79:1525–1531. [PubMed: 28608411]

9. In MH, Posnansky O, Speck O. High-resolution distortion-free diffusion imaging using hybrid spin-warp and echo-planar PSF-encoding approach. NeuroImage. 2017; 148:20–30. [PubMed: 28065851]

10. Zhang Z, Huang F, Ma X, Xie S, Guo H. Self-feeding MUSE: a robust method for high resolution diffusion imaging using interleaved EPI. NeuroImage. 2015; 105:552–560. [PubMed: 25451470]

11. Jeong HK, Gore JC, Anderson AW. High-resolution human diffusion tensor imaging using 2-D navigated multishot SENSE EPI at 7 T. Magn Reson Med. 2013; 69:793–802. [PubMed: 22592941]

12. Ma X, Zhang Z, Dai E, Guo H. Improved multi-shot diffusion imaging using GRAPPA with a compact kernel. NeuroImage. 2016; 138:88–99. [PubMed: 27261163]

13. Robson MD, Gore JC, Constable RT. Measurement of the point spread function in MRI using constant time imaging. Magn Reson Med. 1997; 38:733–740. [PubMed: 9358447]

14. Zeng H, Constable RT. Image distortion correction in EPI: comparison of field mapping with point spread function mapping. Magn Reson Med. 2002; 48:137–146. [PubMed: 12111941]

15. In M-H, Cho S, Shu Y, Min H-K, Bernstein MA, Speck O, Lee KH, Jo HJ. Correction of metal-induced susceptibility artifacts for functional MRI during deep brain stimulation. NeuroImage. 2017; 158:26–36. [PubMed: 28666879]

16. In M-H, Posnansky O, Beall EB, Lowe MJ, Speck O. Distortion correction in EPI using an extended PSF method with a reversed phase gradient approach. PloS one. 2015; 10:e0116320. [PubMed: 25707006]

17. Zaitsev M, Hennig J, Speck O. Point spread function mapping with parallel imaging techniques and high acceleration factors: fast, robust, and flexible method for echo-planar imaging distortion correction. Magn Reson Med. 2004; 52:1156–1166. [PubMed: 15508146]

18. Tuch DS, Reese TG, Wiegell MR, Makris N, Belliveau JW, Wedeen VJ. High angular resolution diffusion imaging reveals intravoxel white matter fiber heterogeneity. Magn Reson Med. 2002; 48:577–582. [PubMed: 12353272]

19. Özarslan E, Mareci TH. Generalized diffusion tensor imaging and analytical relationships between diffusion tensor imaging and high angular resolution diffusion imaging. Magn Reson Med. 2003; 50:955–965. [PubMed: 14587006]

20. Tuch DS. Q-ball imaging. Magn Reson Med. 2004; 52:1358–1372. [PubMed: 15562495]

21. Setsompop K, Gagoski BA, Polimeni JR, Witzel T, Wedeen VJ, Wald LL. Blipped-controlled aliasing in parallel imaging for simultaneous multislice echo planar imaging with reduced g-factor penalty. Magn Reson Med. 2012; 67:1210–1224. [PubMed: 21858868]

22. Breuer FA, Blaimer M, Mueller MF, Seiberlich N, Heidemann RM, Griswold MA, Jakob PM. Controlled aliasing in volumetric parallel imaging (2D CAIPIRINHA). Magn Reson Med. 2006; 55:549–556. [PubMed: 16408271]

23. Polimeni JR, Bhat H, Witzel T, Benner T, Feiweier T, Inati SJ, Renvall V, Heberlein K, Wald LL. Reducing sensitivity losses due to respiration and motion in accelerated echo planar imaging by reordering the autocalibration data acquisition. Magn Reson Med. 2016; 75:665–679. [PubMed: 25809559]

24. Jenkinson M, Beckmann CF, Behrens TE, Woolrich MW, Smith SM. Fsl. NeuroImage. 2012; 62:782–790. [PubMed: 21979382]

25. Andersson JL, Sotiropoulos SN. An integrated approach to correction for off-resonance effects and subject movement in diffusion MR imaging. NeuroImage. 2016; 125:1063–1078. [PubMed: 26481672]

26. Keil B, Blau JN, Biber S, Hoecht P, Tountcheva V, Setsompop K, Triantafyllou C, Wald LL. A 64-channel 3T array coil for accelerated brain MRI. Magn Reson Med. 70:248–258.

27. Blaimer M, Jakob PM, Breuer FA. Regularization method for phase-constrained parallel MRI. Magn Reson Med. 2014; 72:166–171. [PubMed: 23904349]

28. Wang F, Bilgic B, Dong Z, Manhard MK, Ohringer N, Zhao B, Haskell M, Cauley SF, Fan Q, Witzel T, Adalsteinsson E, Wald LL, Setsompop K. Motion-robust sub-millimeter isotropic diffusion imaging through motion corrected generalized slice dithered enhanced resolution (MC-gSlider) acquisition. Magn Reson Med. 2018

29. Dong Z, Wang F, Ma X, Dai E, Zhang Z, Guo H. Motion-corrected k-space reconstruction for interleaved EPI diffusion imaging. Magn Reson Med. 2018; 79:1992–2002. [PubMed: 28771867]

30. Bilgic B, Gagoski BA, Cauley SF, Fan AP, Polimeni JR, Grant PE, Wald LL, Setsompop K. Wave-CAIPI for highly accelerated 3D imaging. Magn Reson Med. 2015; 73:2152–2162. [PubMed: 24986223]

31. Poser BA, Bilgic B, Gagoski BA, Uludağ K, Stenger VA, Wald LL, Setsompop K. Echo-planar imaging with wave-CAIPI acquisition and reconstruction. Proceedings of the 25th Annual Meeting of ISMRM; Honolulu, USA. 2017; Abstract 1198

32. Schwarz JM, Pracht ED, Brenner D, Reuter M, Stöcker T. GRAPPA reconstructed wave-CAIPI MP-RAGE at 7 Tesla. Magn Reson Med. 2018

33. Haldar JP. Low-Rank Modeling of Local k-Space Neighborhoods (LORAKS) for Constrained MRI. IEEE Trans Med Imag. 2014; 33:668–681.

34. Bilgic B, Kim TH, Liao C, Manhard MK, Wald LL, Haldar JP, Setsompop K. Improving parallel imaging by jointly reconstructing multi-contrast data. Magn Reson Med. 2018

35. Setsompop K, Fan Q, Stockmann J, Bilgic B, Huang S, Cauley SF, Nummenmaa A, Wang F, Rathi Y, Witzel T, Wald LL. High-resolution in vivo diffusion imaging of the human brain with generalized slice dithered enhanced resolution: Simultaneous multislice (gSlider-SMS). Magn Reson Med. 2018; 79:141–151. [PubMed: 28261904]
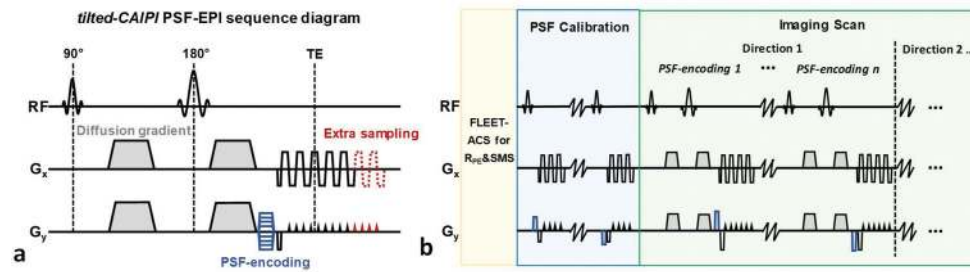
FIG. 1.

(a) The sequence diagram of PSF-EPI with self-navigation. Step-wise PSF-encoding along the phase encoding direction is applied before the EPI readout in a multi-shot manner. At the end of the readout, several extra phase encoding lines are acquired to ensure that the low-frequency k-space data is captured in every PSF-shot to allow for self-navigated phase estimation. (b) The sequence loops of PSF-EPI with calibration and imaging scan.
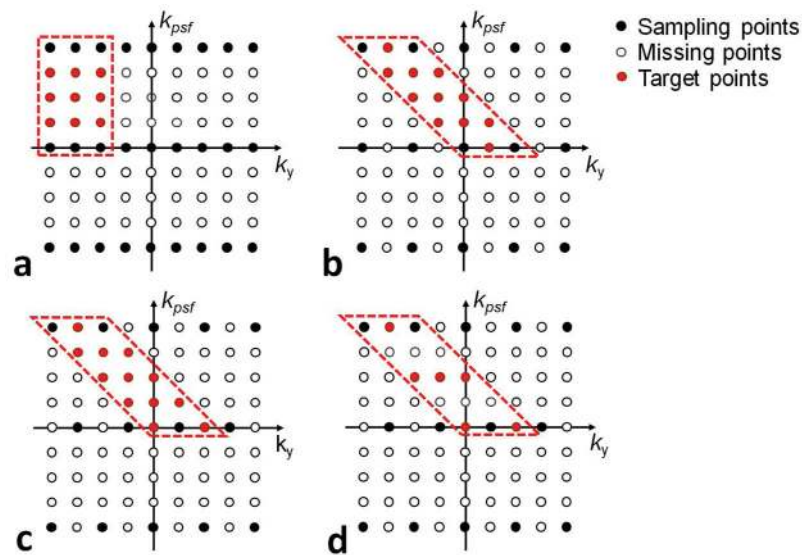
FIG. 2.
Graphical illustration of PSF-EPI and *tilted-CAIPI*. (a) In conventional PSF-GRAPPA, a square kernel is used to reconstruct the missing signals along the PSF-encoding dimension after the under-sampling along k_y is recovered by PE-GRAPPA. (b) Here, a tilted kernel is proposed to take advantage of the strong signal correlation of the PSF-PE dimension through joint PSF-PE reconstruction. (c) Sampling along k_y is shifted to achieve an optimized *tilted-CAIPI* pattern for parallel imaging. (d) To reduce the number of kernel sets that needs to train and accelerate the calibration scan, only a sub-set of the k_{psf} lines are reconstructed by PSF-GRAPPA, while the remaining aliasing in *y-psf* is unfolded in image domain using rFOV unfolding.
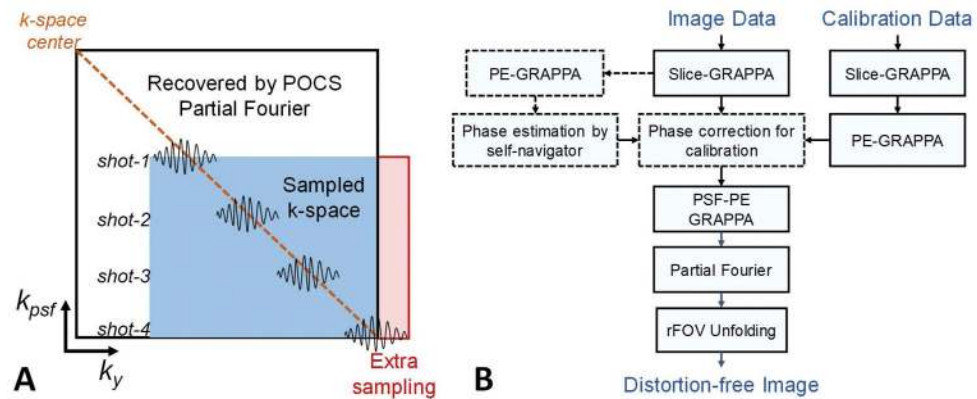
FIG. 3.

(A) Illustration of the proposed self-navigation approach for the application of PSF-EPI in diffusion imaging. Several PSF-encodings (k_{psf}) are acquired with partial Fourier, each contains a portion of low-frequency signals to allow for self-navigation (acquired data shown in blue, with low-frequency data shown as wiggly signals). The extra sampling of the phase encoding at the end of each readout (right-edge in red) enables self-navigation for acquisition shots with large PSF-encodings. (B) Flowchart of the overall reconstruction process. The steps in the dashed boxes are only applicable for diffusion imaging where phase correction is needed. Calibration data is acquired using non-diffusion-weighted PSF-EPI for PSF-PE GRAPPA training. Slice-GRAPPA and PE-GRAPPA are applied to recover low-resolution images to estimate the diffusion-induced phase. Distortion-free images can then be reconstructed by PSF-PE GRAPPA with phase-corrected kernel training.
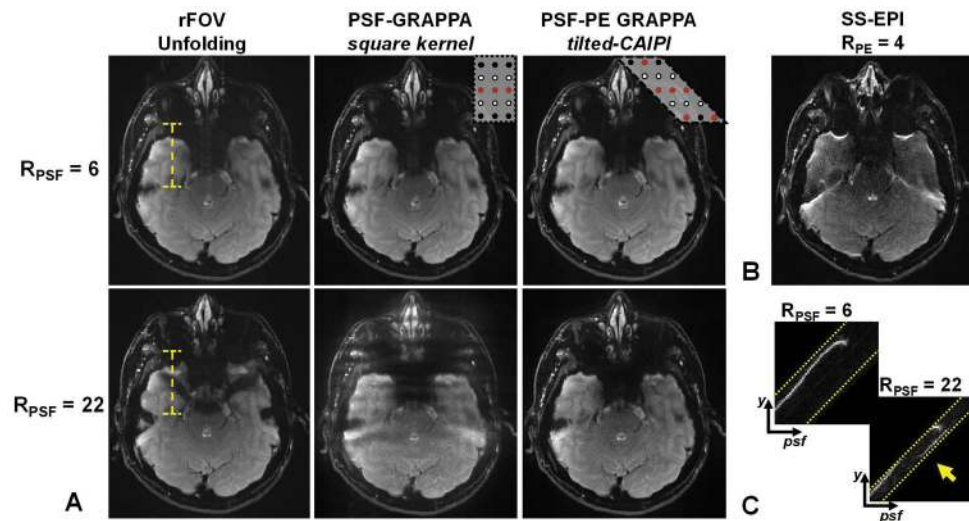
FIG. 4.

(A) Image reconstruction results at $R_{PSF} = 6$ (top) and $R_{PSF} = 22$ (bottom) for i) reduce-FOV unfolding, ii) PSF-GRAPPA with a square kernel, and iii) PSF-PE GRAPPA with *tilted-CAIPI*. $R_{PE} = 4$ was employed for all cases. The examples of the sampling patterns for the square and the *tilted-CAIPI* kernels are shown at the top-right of their corresponding images (first row). All methods performed well at $R_{PSF} = 6$, while only the tilted-CAIPI method provides artifact-free reconstruction at $R_{PSF} = 22$. Panel (C) provides a zoomed-in region of the *y-psf* view from images of rFOV unfolding (yellow dashed lines in A), where limited diagonal regions (between the two diagonal dashed lines) were reconstructed to resolve the aliasing artifacts due to under-sampling. The fold-over structures in the zoomed-in view explains the aliasing artifacts in the rFOV unfolding reconstruction at $R_{PSF} = 22$. Panel (B) shows that single-shot EPI acquisition with $R_{PE} = 4$ and effective ESP of 0.245ms still results in severe distortion artifacts for this slice with large B_0 inhomogeneity.
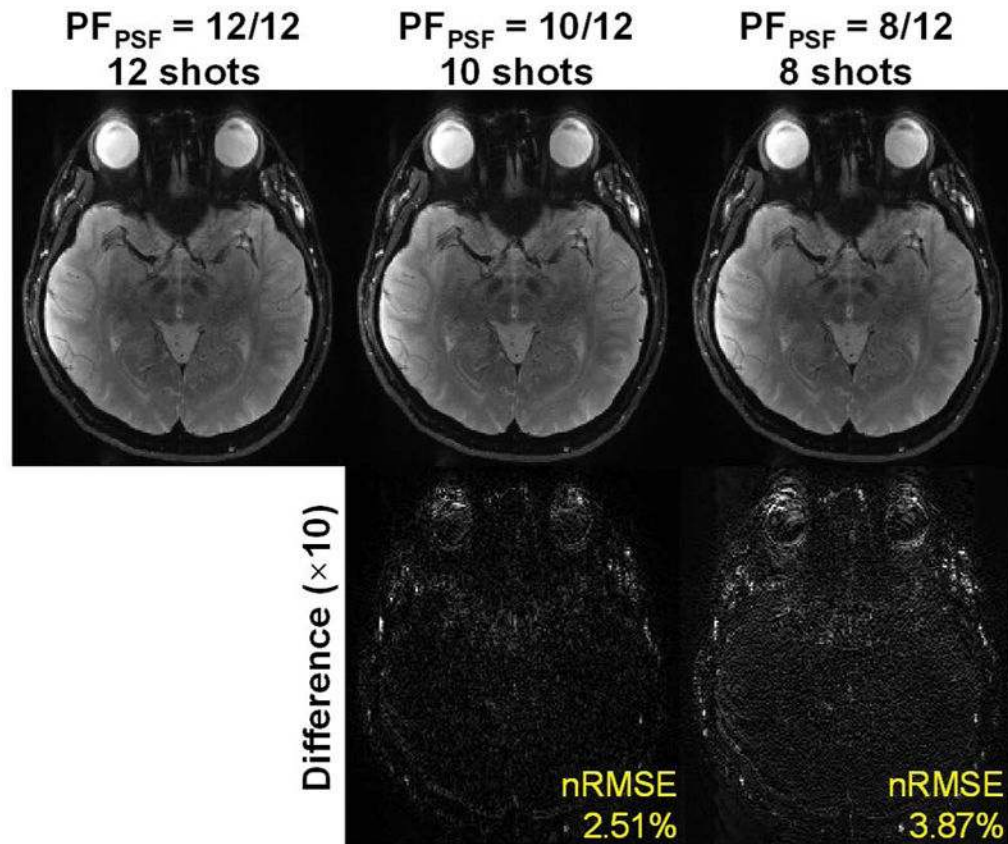
FIG. 5.

Results of partial Fourier acquisition and reconstruction. The data (Table 1, scan 1) were retrospectively undersampled with different PSF partial Fourier factors of 8/12, 10/12 and 12/12. In all cases, $PF_{PE} = 0.75$ and $R_{PSF} = 22$ were used. The under-sampling of PSF (R_{PSF}) was reconstructed by PSF-PE GRAPPA first. Then, both PE and PSF partial Fourier were reconstructed using POCS. The difference maps (×10) between partial Fourier reconstructions and the case at $PF_{PSF} = 12/12$ are shown. The image errors are small (nRMSE < 4%) at $R_{PSF} = 10/12$ and 8/12.
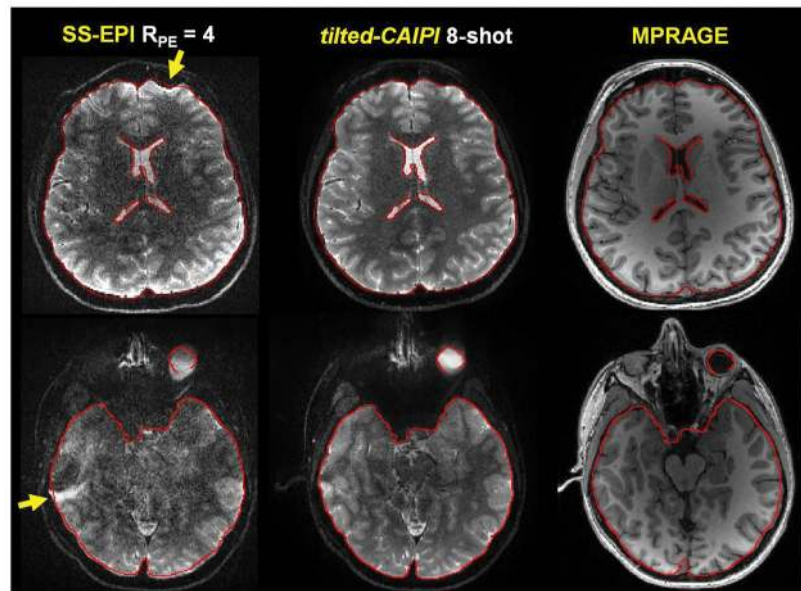
FIG. 6.

$0.9{\times}0.9{\times}1\ mm^3$ whole-brain T_2-weighted scan (Table 1–2) using SS-EPI and PSF-EPI. Two representative slices are shown, along with corresponding distortion-free MPRAGE images at the same slice positions. Here, SS-EPI was acquired with $R_{PE} = 4$, but still has severe distortion (yellow arrows) when compared with the distortion-free MPRAGE. In contrast, the brain boundary of PSF-EPI and MPRAGE are identical. This demonstrates the ability of PSF-EPI with *tilted-CAIPI* to achieve distortion-free imaging with improved SNR even when very high accelerations are employed ($R_{PE}{\times}MB = 4{\times}2$, $R_{PSF} = 22$, PSF partial Fourier $= 0.67$).
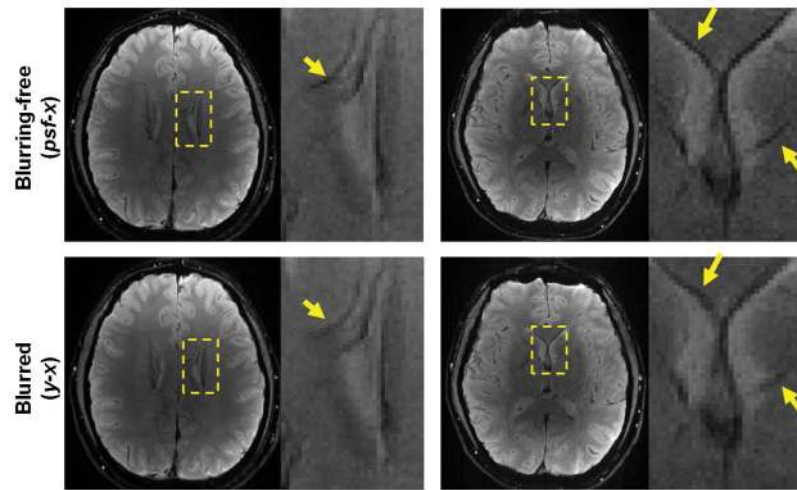
FIG. 7.
$0.8 \times 0.8 \times 1 \text{ mm}^3$ whole-brain T_2^*-weighted imaging (Table 1–3) by *tilted-CAIPI* PSF-EPI. The *psf-x* images were obtained by performing SOS along *y*, while the *y-x* images were obtained by SOS along *psf*. As shown in the zoomed-in regions (dashed squares), images in the *psf-x* plane achieved higher resolution than those in the *y-x* plane that suffer from blurring artifacts (yellow arrows) even using $R_{PE}=4$ for blurring reduction.
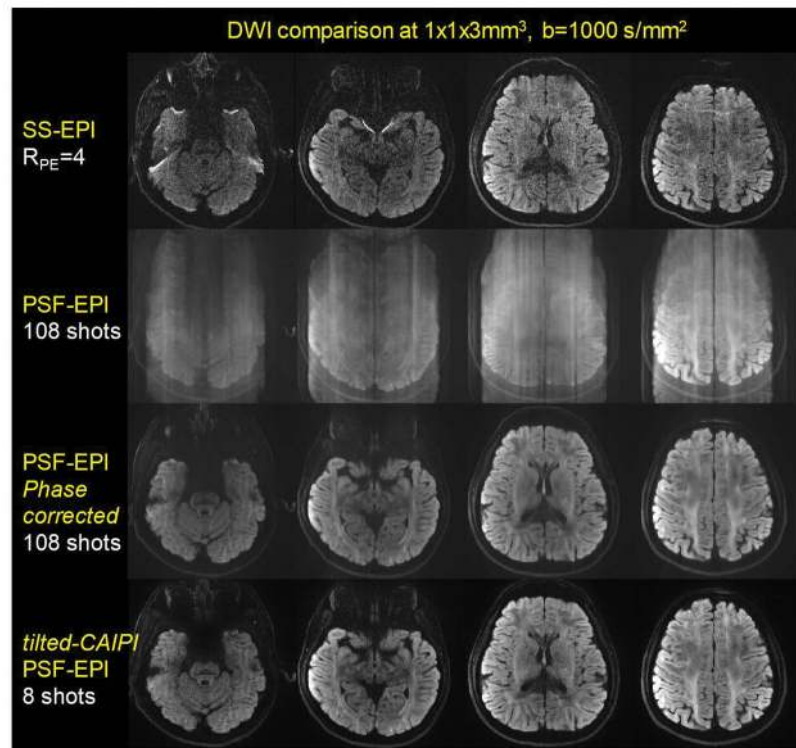
FIG. 8.
Comparison between SS-EPI, PSF-EPI, and highly-accelerated PSF-EPI with *tilted-CAIPI* in DWI. As shown in this figure, PSF-EPI eliminates the susceptibly-induced distortion along phase encoding direction that is present in SS-EPI, while the strong aliasing artifacts were effectively removed by the proposed phase correction using self-navigation. The 8-shot acquisition using *tilted-CAIPI* resulted in distortion-free DW images with high SNR, which shows close image quality to the 108-shot case, but with a much shorter acquisition time.
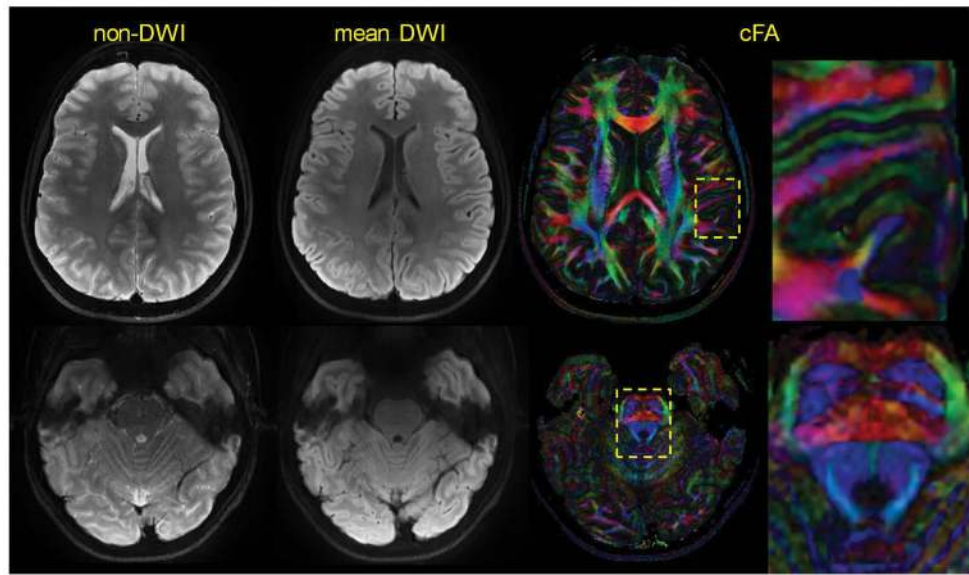
FIG. 9.
Results of 0.8×0.8×3 mm^3 48-direction diffusion scan at b=1000 s/mm^2 (Table 1, scan 4). Distortion-free non-DW images, mean DW images, and color-coded FA maps are shown at two representative slices. The proposed method achieved high-resolution high-SNR diffusion imaging that can nicely elicit detailed brain structures as shown in the zoomed-in regions (yellow dashed squares). The scan time of 8-shot distortion-free acquisition was 24s/per diffusion direction, and the total scan time was about 20 minutes.

Table 1

Acquisition parameters of the in-vivo experiments.

	Scans	Resolution x-psf (mm²)	FOV (mm²)	Matrix size (x-y)	Slice thickness (mm)	Slice number	TR/TE (ms)	Partial Fourier (PE/PSF)	R_{PE}/R_{PSF}	PSF steps	MB	b-value (s/mm²)	Diff. direction	Tesp/ effective Tesp (ms)	Scan time
1	DWI/b0	1 × 1	216×216	216×216	3	5	2000/58	0.75/1	4/2	108	1	1000	4	0.98/0.245	15min24s
	calibration	3.4×3.4	216×216	64×64	3	5	2000/32	1/1	2/2	14	1	0	/	0.49/0.245	28s
2	T_2-w	0.9×0.9	220×220	244×244	1	126	6400/56	0.75/0.67	4/22	8	2	0	/	0.98/0.245	52s
	calibration	2.4×2.4	220×220	90×90	1	126	4700/47	1/1	2/2	14	2	0	/	0.49/0.245	66s
3	T_2^*-w	0.8×0.8	198×198	244×244	3	46	1900/28	0.75/0.67	4/22	8	2	0	/	1.15/0.29	15s
	calibration	2.2×2.2	198×198	90×90	3	46	1100/20	1/1	2/2	14	2	0	/	0.58/0.29	16s
4	DTI	0.8×0.8	198×198	244×244	3	46	3000/67	0.75/0.67	4/22	8	2	1000	48	1.08/0.27	19min12s
	calibration	2.2×2.2	198×198	90×90	3	46	2000/49	1/1	2/2	14	2	0	/	0.54/0.27	28s
5	Phantom	0.8×0.8	198×198	244×244	3	46	4200/96	0.75/0.67	2/22	8	2	1000	48	1.08/0.54	26min53s
	calibration	2.2×2.2	198×198	90×90	3	46	2700/74	1/1	2/2	14	2	0	/	0.54/0.54	38s